Unbiased Gradient Estimation for Differentiable Surface Splatting via Poisson Sampling

Jan U. Müller[1], Michael Weinmann[2], and Reinhard Klein[1]

[1] Institute of Computer Science, University of Bonn, Germany
[2] Department of Intelligent Systems, Delft University of Technology, Netherlands

Abstract. We propose an efficient and GPU-accelerated sampling framework which enables unbiased gradient approximation for differentiable point cloud rendering based on surface splatting. Our framework models the contribution of a point to the rendered image as a probability distribution. We derive an unbiased approximative gradient for the rendering function within this model. To efficiently evaluate the proposed sample estimate, we introduce a tree-based data-structure which employs multipole methods to draw samples in near linear time. Our gradient estimator allows us to avoid regularization required by previous methods, leading to a more faithful shape recovery from images. Furthermore, we validate that these improvements are applicable to real-world applications by refining the camera poses and point cloud obtained from a real-time SLAM system. Finally, employing our framework in a neural rendering setting optimizes both the point cloud and network parameters, highlighting the framework's ability to enhance data driven approaches.

Keywords: Differentiable rendering · Point cloud · Multipole method · Shape recovery · Scene reconstruction

1 Introduction

Inverse rendering, i.e. the inference of scene parameters such as scene geometry, reflectance or illumination as well as imaging parameters based on observations [4], has become a central problem in Computer Vision and Graphics. A wide range of applications utilize inverse rendering; including reflectance estimation [47], object reconstruction, face remapping, body pose estimation and teeth modeling [23]. Additionally, inverse rendering can improve scene understanding in robotics [57] and can be applied to a variety of problems in Geodesy [12]. A current approach that receives a lot of attention from the research community is differentiable rendering. It describes rendering methods that provide a gradient of a rendering function with respect to scene and imaging parameters, which promises a general purpose solution to the inverse rendering problem. Intuitively, the gradient conveys information about how parameters have to be changed to match a reference observation. The potential of this approach has led to the development of a variety of differentiable rendering algorithms, categorized by rendering technique or geometry representation: differentiable light transport

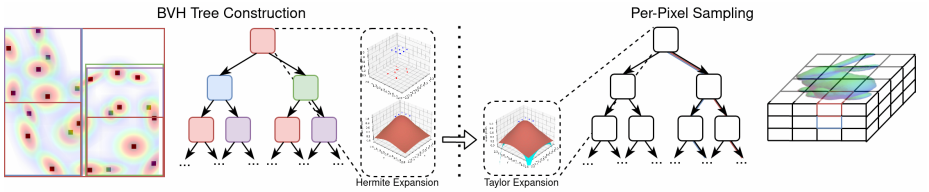

Fig. 1: Illustration of our proposed algorithm to draw per-pixel samples while still scaling linear with respect to image and point cloud size. The construction steps builds a BVH tree and computes Hermite coefficients on the GPU. Afterwards the tree is traversed for each pixel in parallel and the Hermite coefficients are used to identify points with a high contributions to the pixels. Hermite coefficients might be converted into Taylor expansions to improve performance.

[44, 49, 40], implicit neural representations [41], voxel-based [20, 37, 69], mesh-based [39, 36, 30] and point-based representations [66, 61, 31]. Differentiable light transport uses Monte-Carlo sampling which makes the approach computationally expensive. Recent advances made NeRF approaches real-time capable [42], however, these techniques are view synthesis methods and currently do not focus on generalization between scenes. Voxel-based methods can be combined with 3D-CNNs to augment data-driven approaches [60, 17, 37, 20], however, voxel methods are memory constrained which prevents accurate representation of fine geometric details. Differentiable rendering of mesh representations [39, 25, 36, 30] is more scalable but is constrained by the discrete topology of meshes which requires a work-around to allows for strong shape deformations.

Our approach relies on point-based representations, which do not require the initialization to approximate the final topology and are memory efficient compared to voxel-based representations. The method interprets a Gaussian kernel in a point's tangent space, which was introduced in surface splatting [16, 77], as a probability density of the points' influence on the overall image. Our method does not require a truncation of the kernels to allow for efficient rendering but instead adapts the concept of importance sampling to point cloud rendering. Without a truncation step there are fewer discontinuities in our rendering pipeline. Importantly, our stochastic interpretation allows to derive an unbiased gradient estimator which is not limited to a local region around each point but approximates the gradient over the complete image space. This allows our method to overcome the major challenge of defining an useful surrogate gradient which often requires additional regularization. Previous methods only accumulate local gradients around a surfel [61, 31] or rely on a finite-differences surrogate gradient [66]. To efficiently evaluate our sample estimate, we augment a radix-tree [22] to provide an approximation of cumulative inclusion probabilities via Hermite expansions. This yields a space partitioning scheme that is used to draw samples for each pixel while scaling linearly with instance size. An overview of this framework is presented in Figure 1. Furthermore, it is designed with the constraint of

shared-memory multiprocessors in mind, consequently maps well to GPUs and is publicly available[1]. Our overall contributions can be summarized as:

- We introduce a stochastic interpretation of surface splatting that abstains from kernel truncation and the resulting discontinuity. This interpretation allows us to derive an unbiased estimator for the sampling based renderer without relying on surrogates such as finite-differences [66] or sub-gradients [61].
- The proposed sampling algorithm used to generate the necessary samples per pixel scales near linearly with respect to the image size and number of points. By design, it allows parallelization of data processing and maps well to the constraints of shared memory multiprocessors, which allows for a GPU-accelerated implementation.
- We demonstrate that our approach yields a differentiable renderer that does not require regularization and improves the fidelity of shape reconstructions over current point-based differentiable rendering methods. We further demonstrate the framework's flexibility by exploring its use to improve scene reconstruction and train it in conjunction with a neural network.

2 Related Works

In this section, we briefly review work on the topics of differentiable rendering and discrete Gaussian transform approximation.

Differentiable Rendering A large body of work exists which proposes application-specific methods that can be classified as differentiable rendering [27, 53, 71, 63, 74, 1, 21]. However, these methods use domain-specific knowledge whereas our approach is not limited to a specific application. Another parallel research direction is differentiable simulation of light transport via computationally expensive Monte-Carlo estimation to render images and propagate the gradients [44, 43]. Recently, this method has been extended to also provide a gradient for any scene parameter including geometry and camera parameters [73, 3, 72, 40]. In this work, we focus on fast shape recovery from RGB images and integration into deep neural networks, instead of using more computationally expensive differentiable light transport techniques. In the remainder of this paragraph, we focus on related work that is comparable to our method.

Voxel, Signed distance (SDF) and Implicit Representations Early approaches use a differentiable projection to obtain a silhouette from a voxel grid [64, 76, 75]. Recent approaches use differentiable ray marching through a density voxel field [64, 76, 75] or sphere tracing in an opaque voxel field [20]. However, voxel-based representations require large amounts of memory in order to represent fine geometric details. Deformations of the voxel-grid have been explored to address this drawback [37, 8, 38]. "Neural Radiance Field" (NeRF) [41] has been demonstrated to reproduce finer details with a smaller memory footprint and has been improved by increasing inference performance [13, 51, 69], making

[1] https://github.com/muellerju/unbiased-differentiable-splatting

it real-time capable [42, 70] or enabling scene relighting [58, 7]. Point-based representations are more memory efficient than dense voxel-grids and scale to larger scenes without workarounds. Furthermore, our point based method can be incorporated into deep neural networks as opposed to real-time "NeRF" approaches for which the integration into neural networks appears to be non-trivial since they are designed for novel view synthesis of individual scenes. In addition, our rendering pipeline does not entangle geometry and reflectance representations which significantly simplifies scene relighting.

Mesh-based Representations Mesh-based representations have non-continuous boundaries that can be circumvented with surrogate gradients [39, 25] which require regularization to avoid object shrinkage [24]. The "Soft Rasterizer" [36] proposes a probabilistic approximation of the rendering pipeline and has been improved to enable optimization of diffuse shading [48, 10] and to increase performance [49]. Recently, flexible mesh-based differentiable rendering frameworks have been introduced [50] which includes hardware accelerated deferred rendering [30]. However, mesh-based differentiable renderers have been demonstrated to be unable to perform complex deformations [66]. This is an inherent problem of their discrete topology, which does not exist in an unstructured point cloud. Similar to the "Soft Rasterizer" [36], our proposed method uses a probabilistic interpretation to mitigate discontinuities. However, the our sampling method avoids the quadratic scaling of the "Soft Rasterizer" and has a lower variance than mesh rendering which uses uniform sampling [52]. Our implementation does not utilize any graphics hardware specific instructions, which allows it to be run on any general purpose computing hardware.

Point-based Representations Several point-based methods have been proposed which do not present a general purpose renderer [34, 18, 54]. Smoothed boundary approaches similar to the "Soft Rasterizer"[36] have only been demonstrated to render low resolution patches [33] or truncate the smoothed boundary to render full images but use a sub-gradient approximation at the boundary [61]. "Pulsar" [31] associates a sphere with each point similar to [33] but proposes a more efficient acceleration structure. In contrast to these surfel methods, our method also takes the surface normal into consideration which allows for a more accurate representation of a surface given the same number of points. "Differentiable surface splatting" (DSS) [66] adapts surface splatting [77] into a general differentiable renderer by introducing a surrogate gradient. In our evaluation, we will highlight that our stochastic framework yields a more faithful shape recovery compare to previous methods. Additionally, our unbiased estimator avoids the use of expensive finite-differences surrogate gradients [66] which enables its application to room-scale scenes. Several works combine point-rendering with neural rendering [2, 55, 29]; either by rendering pixel-sized points [2, 55] or by utilizing DSS in "Point-based neural graphics" [29]. Pixel-sized methods render sparse images at multiple resolutions and require a rendering network to perform hole-filling. This necessitates a per-scene training of the rendering network whereas our method allows for direct optimization of large-scale scenes. Since we improve upon results obtained with DSS and demonstrate that our method can

be used in conjunction with a neural rendering network, our framework should be a drop-in replacement into the "Point-based neural graphics" pipeline.

Discrete Gaussian Transform Approximation The discrete Gaussian Transform (DGT) is a finite mixture of Gaussians (whereas a Gaussian mixture model is a convex combination). "Fast Gaussian Transform" [15] proposes a "fast multipole method" (FMM) based on Hermite and Taylor expansions and a spatial grid to approximate the DGT for large numbers of source and target points in linear time. Subsequent works proposed improvements to the spatial datastructure [14, 65, 32] and generalize to larger classes of kernel functions [11, 56]. In particular, [32] proposes the use of a dual kD-tree and a coupled traversal of both trees to evaluate the DGT. More recently, task-based threading models have been proposed to improve throughput on CPUs [68] and shared memory architectures [35, 62]. Our algorithm builds on previous ideas [15, 32], however, we adapt these concepts to not only provide an approximation of DGT at the root node but potentially at every node in the source tree. Furthermore, we employ domain-specific knowledge by replacing the target-tree with a grid structure, since the pixels are uniformly distributed. Lastly, we use a BVH-tree that can be efficiently constructed on the GPU [22] to store source points, which is in contrast to previous techniques [35, 62] that only accelerate the traversal with GPUs.

3 Statistical Splatting with Unbiased Gradient Estimator

In our rendering algorithm we avoid the additional discontinuity that comes with truncating the Gaussian kernel introduced in "surface splatting" [77]. This removes the bias that leads to shrinkage in previous "DSS" [66]. However, a naive evaluation of the complete Gaussian kernel scales quadratic (i.e. number of pixels times number of points); to obtain an efficient renderer we approximate pixel and gradient values using unbiased sample estimates. "Surface splatting " is a resampling framework for aliasing-free point cloud rendering that associates each point with a resampling kernel $\rho_k(x)$. This kernel is approximated by projecting a Gaussian basis function from a point's tangent plane into screen-space. Let $\mathcal{N}_x$ be the set of points that describe the surface at a pixel x and f_k an attribute value for each point k (e.g. albedo color). Surface splatting computes the pixel value $f_c(x)$ at position x as the weighted sum of pixel contributions:

$$f_c(x) := \sum_{k \in N_x} f_k \rho_k(x) \text{ with } \rho_k(x) := \frac{1}{|J_k^{-1}|} G_{J_k V_k J_k^T + I}(x - m(u_k)) \qquad (1)$$

where $m(u_k)$ is the projection of the point position u_k into screen space, J_k^{-1} is the Jacobian of the camera transformation and perspective projection, V_k is a diagonal matrix to control the splat sizes and $G_A(x)$ is the multivariate Gaussian density function with covariance matrix A. For more details, we refer to Zwicker et al. [77]. Previous methods [77, 78] truncate the Gaussian kernel $\rho_k(x)$ to obtain an elliptical splat. Limiting the Gaussian kernel to have a local support

decreases the algorithm's runtime but requires a finite-differences approach [66] to compute a gradient. In the following, we detail a stochastic framework used in the forward and backward pass as well as an algorithm to efficiently evaluate this framework.

Forward Pass First, we identify a set of candidate points which could have an effect on the pixel's filtered attribute value without taking occlusion into consideration. We propose to draw this set of points $\tilde{\mathcal{N}}_x$ for each pixel x by sampling without replacement (SWOR) such that the inclusion probability of point k at pixel x is proportional to its influence on the pixel: $\tilde{p}_k(x) \sim f_k \rho_k(c)$. Afterwards, our method evaluates the contributions of the sampled points $\tilde{\mathcal{N}}_x$ at pixel x according to Equation 1 and resolves the occlusion in a depth filtering step to determine the set of visible points $\mathcal{N}_x$. Our algorithm uses an alpha-blending method, which was originally introduce by Zwicker et al. [78], to perform the depth-filtering. The alpha-based methods sorts the points in $\tilde{\mathcal{N}}_x$ by descending distance from the camera and accumulates the contributions of a point such that its contribution is at most one minus all previous contributions. Wiles et al. [61] have demonstrated that alpha-blending yields an improved gradient propagation compared to the z-Buffer approximation in DSS [66].

Backward Pass Second, our novel backward pass utilizes of an unbiased estimator to compute the gradient using the samples computed during the forward pass as follows: Let $\mathcal{L}$ be a differentiable image loss function. The derivative of a point parameter ω_k (e.g. position or normal) can be computed by accumulating its derivative over the complete image

$$\frac{\partial \mathcal{L}}{\partial \omega_k} = \sum_x \frac{\partial \mathcal{L}}{\partial f_c(x)} \frac{\partial f_c(x)}{\partial \omega_k}. \tag{2}$$

However, at pixel x we only consider the points in $\tilde{\mathcal{N}}_x$ which have been drawn by SWOR such that $P(k \in \tilde{\mathcal{N}}_x) = \tilde{p}_k(x)$. To obtain an unbiased estimator for Equation 2, we make the following observations: First, the set of pixels $\mathcal{N}_k := \{x \mid k \in \tilde{\mathcal{N}}_x\}$ that are influenced by point k contains no duplicates, since $\tilde{\mathcal{N}}_x$ was drawn with SWOR and does not have any duplicates. Second, the probability that a pixel is included in $\mathcal{N}_k$ is equal to $P(k \in \tilde{\mathcal{N}}_x)$ by construction. Finally, note that the size of the set $\mathcal{N}_k$ is a random variable. This allows us to use a modified Horvitz–Thompson estimator [9] to approximate the derivative in Equation 2 as

$$\frac{\partial \mathcal{L}}{\partial \omega_k} \approx \frac{1}{|\mathcal{N}_k|} \sum_{x \in \mathcal{N}_k} \frac{1}{\tilde{p}_k(x)} \frac{\partial \mathcal{L}}{\partial f_c(x)} \frac{\partial f_c(x)}{\partial \omega_k} \tag{3}$$

if $|\mathcal{N}_k| > 0$ and $\partial \mathcal{L}/\partial \omega_k = 0$ otherwise. Note that the inclusion probability is not strictly proportional-to-size, since $\tilde{p}_k$ is not scaled according to the loss derivative $\partial \mathcal{L}/\partial \omega_k$. However, the gradient is dominated by the exponential decay of the Gaussian kernel $\rho_k(x)$ that outweighs the unaccounted scaling term even for pixels close to a point.

3.1 Efficient Pixel-wise Sampling

Algorithm 1: Our adaption of the Sequential Poisson sampling algorithm to generate a sample for each pixel in parallel.

for all all pixels x in parallel **do**
  Let S_x be an empty list of size s to store sampled indices.
  Initialize $\xi = \infty$ the upper bound of transformed random numbers.
  while $\epsilon \leq \xi \cdot c_{x,r} \cdot \sigma_r(x)$ **do**
    Let n be the root of the tree T with point indices $I_n \subseteq [1:N]$.
    while $|I_n| > m$ **do**
      Let n_l, n_r be the left and right child node of n.
      Set $n \leftarrow n_l$ if $c_{x,n_l}\sigma_{n_l}(x) > c_{x,n_r}\sigma_{n_r}(x)$ else set $n \leftarrow n_r$.
    Compute and sort ξ_k in ascending order for all $k \in I_n$.
    Merge I_n with S_x to obtain a SPS sample.
    Set $\xi \leftarrow \max_{k \in S_x} \xi_k$.
    Initialize the path probability $\beta = 1$.
    while n is not the root **do**
      Update the capacity $c_{x,n} \leftarrow \max\{0, c_{x,n} - \beta\}$.
      Let n' be the node which shares a parent with the node n.
      Set $\beta \leftarrow \beta \cdot \frac{\sigma_n(x)}{\sigma_n(x)+\sigma_{n'}(x)}$ and $n \leftarrow \text{parent}(n)$.

In order to evaluate our sampling-based splatting framework efficiently we introduce a tree-based sampling algorithm that serves two purposes: First, the algorithm allows to approximate the total contribution $f_c(x)$ of all points at each pixel x (i.e $\mathcal{N}_x = [1:N]$) which allows for proportional-to-size sampling in the forward step. Second, it allows us to draw the set $\tilde{\mathcal{N}}_x$ for each pixel and provide the inclusion probabilities of points within the samples.

In order to achieve these objectives, our algorithm utilizes a fast multipole method (FMM) [15, 32] which was originally introduced for N-body simulations to approximate a sum of Gaussians (DGT) at multiple points in linear instead of quadratic time. The idea of FMM is that a DGT of nearby points can be approximated with a truncated Hermite expansion which provides a global approximation. This Hermite expansion can be converted into a truncated Taylor expansion, which approximates the DGT only locally but is more efficient to evaluate for multiple points:

$$f_c(x) \approx \underbrace{\sum_{0 \leq \alpha \leq n} A_\alpha h_\alpha \left(\frac{x - x_H}{\sqrt{2h^2}} \right)}_{\text{truncated Hermite expansion}} \text{ and } f_c(x) \approx \underbrace{\sum_{0 \leq \beta \leq n} B_\beta \left(\frac{x - x_T}{\sqrt{2h^2}} \right)^\beta}_{\text{truncated Taylor expansion}}$$

where $h_\alpha = e^{-t^2} H_\alpha(t)$ is a Hermite function of the Hermite polynomial H_α, A_α are the coefficients of a truncated Hermite expansion at point X_H which can be converted into coefficients B_β of a truncated Taylor expansion at point X_T and h is the Gaussian's bandwidth parameter. For details on computing and converting the coefficients we refer to *Lee et al.* [32]. Since FMM assumes isotropic Gaussians with bandwidth h, we derive a best fit bandwidth for the multivariate Gaussians. For further details on this step we refer to the supplemental.

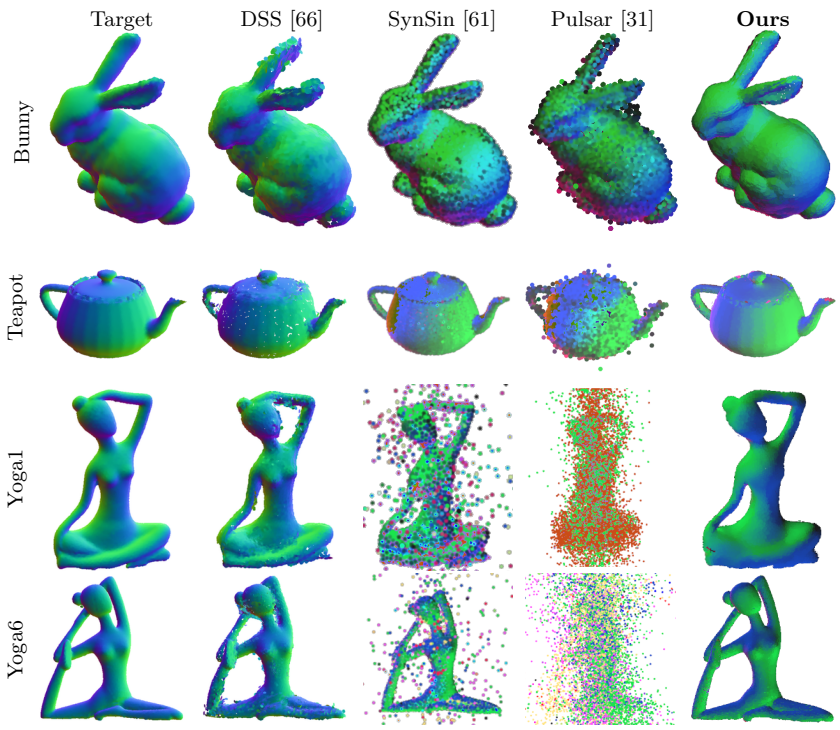

Fig. 2: Shape reconstruction from images using the proposed method compared to results obtained using previous methods. Our method exhibits fewer outliers, more accurate normal directions and an improved reconstruction of extremities. Images were rendered after converged optimization based on the lighting conditions used in Yifan et al [66], which was not provided but manually recreated.

Tree Construction For each batch of points, we construct a bounding-volume-hierarchy (BVH) tree using a radix-sort based algorithm [22]. The algorithm enables the BVH-tree construction in near linear time on the GPU. We extend the last step of the construction in this algorithm which propagates the bounding-boxes (BB) from leafs to the root, to also compute an Hermite expansion for each node within the tree: If the nodes' BB has a side length smaller than $2h$ a Hermit expansion can be computed. The expansion point X_H is chosen to be the average of the child nodes' expansion points and the Hermite degree is increased until the approximation error is smaller than a user-defined threshold ϵ. Finally, the Hermite coefficients of the children are shifted and accumulated at the new expansion point. Otherwise, the BB side length is greater or equal to $2h$ and the node is marked to have no valid Hermite expansion. The shift operation between nodes, bound for the approximation error have been established by Lee et al. [32] for the use in dual-trees. In contrast to this method, our algorithm computes

Dataset	Bunny		Teapot		Yoga1		Yoga6	
	HD ↓	CD ↓	HD ↓	CD ↓	HD ↓	CD ↓	HD ↓	CD ↓
DSS [66]	7.73	1.817	12.766	1.586	14.039	6.351	12.631	3.84
SynSin [61]	75.806	4.074	13.019	4.771	7375.3279	572.224	7861.088	344.151
Pulsar [31]	4.463	1.371	17.036	15.478	25241.71	7746.145	43641.085	12621.735
Ours	**0.442**	**0.125**	**0.453**	**0.289**	**3.355**	**1.385**	**1.551**	**0.517**

Table 1: Quantitative comparison between the reconstructed and ground-truth pointsets using the Hausdorff (HD) and Chamfer (CD) distance. Our method with non-visible point repositioning outperforms previous methods significantly. The values are an average of 10 runs with a maximum std. deviation of at most 0.0121. Further details are provided in the supplemental.

the Hermite coefficients during the tree construction in parallel whereas Lee et al. [32] only compute the coefficients during sequential depth first traversal.

Sampling Poisson sampling performs sampling without replacement and by design provides an element's inclusion probability. Therefore it satisfies the requirements introduced by our gradient estimator in Equation 3, but its sample size is a random variable which is not well-suited for regular shaped tensor objects used in deep-learning frameworks. Instead we generate the samples by adapting sequential Poisson sampling (SPS), which returns a fixed size sample with user specified size m and has been demonstrated empirically to approximate proportional-to-size sampling without replacement [45]. SPS computes a transformed random number $\xi_{x,k} = u_{x,k}/\tilde{p}_k(x)$ where $u_{x,k}$ is a uniform sample between $[0, 1]$ and returns the indices which have the m smallest transformed random numbers. However, drawing a SPS sample for each pixel with this naive algorithm has at least quadratic runtime.

Our algorithm returns a sample and its inclusion probability for each pixel, which has size m and is with probability $1 - \epsilon$ a SPS sample. The algorithm searches for nodes in the tree which have a high likelihood to include points that are contained in a SPS sample and merges them with the current sample. It terminates if the likelihood of all remaining points to be in a SPS sample is smaller than a user-defined threshold ϵ. The search traverses the tree from the root to leaf by choosing the node n with the largest cumulative probability $\sigma_n(x) = \sum_{i \in I_n} f_k \rho_k(x)$ where I_n are the indices of points contained in node n. We describe the evaluation of $\sigma_n(x)$ in the next paragraph. Duplicate samples are avoided by reducing the capacity $c_{x,n}$ along the path. Our parallel SPS procedure is described in detail in Algorithm 1. The runtime of our algorithm is a random variable. Our algorithm scales linearly in an average case, since the expected likelihood for a point to be included in the SPS drops exponentially with distance to a pixel. For a detailed analysis we refer to the supplemental.

Approximating Cumulative Inclusion Probabilities Our implementation of Algorithm 1 maps each pixel to a thread on the GPU. We choose this mapping such that a thread-block processes a rectangular block of pixels whose size is chosen to maximize processor occupancy. We utilize this spatial relationship

Fig. 3: Comparison between test images in the dataset by Mildenhall et al. [41] and the inference from the neural renderer which uses our method as an intermediate layer. The dataset was scaled to 256×256 pixels due to limited hardware.

by pre-computing Taylor expansions for nodes that are close to the root. In a pre-processing sub-routine to Algorithm 1 the first k' threads within a block compute a Taylor expansion for the first k' nodes in level order and store them in shared memory. The number of pre-computed Taylor coefficients depends on the available shared memory. This accelerates the evaluation of the CDF $\sigma_n(x)$ for frequently visited nodes during the execution of Algorithm 1. After the pre-processing step Algorithm 1 is executed and uses the following heuristic to select between the evaluation techniques:

- The thread searches via linear probing for Taylor coefficients of node n in shared memory. If a local expansions exists, it is used to evaluate $\sigma_n(x)$.
- Otherwise, if node n has a valid Hermite expansion, its Hermite coefficients are used to evaluate the CDF.
- If the node has neither expansion, the algorithm traverses the sub-tree and evaluates the Hermite expansions of the nodes' children to compute the CDF.

Implementation Our framework is implemented as two CUDA extensions for "PyTorch" [46] where each extension combines multiple kernels. An implementation as a custom "PyTorch" extension provides flexibility when exploring the choice of optimizer, learning rate schedule or loss function. It further allows our method to be easily combined with existing neural network building blocks. The majority of the extensions are written as native CUDA kernels in CUDA-C and use the "PyTorch" C++ wrapper to provide memory management as well as a Python wrapper; only the construction of the tree is implemented using the "Thrust" library [5]. We keep track of the capacity values for each pixel and

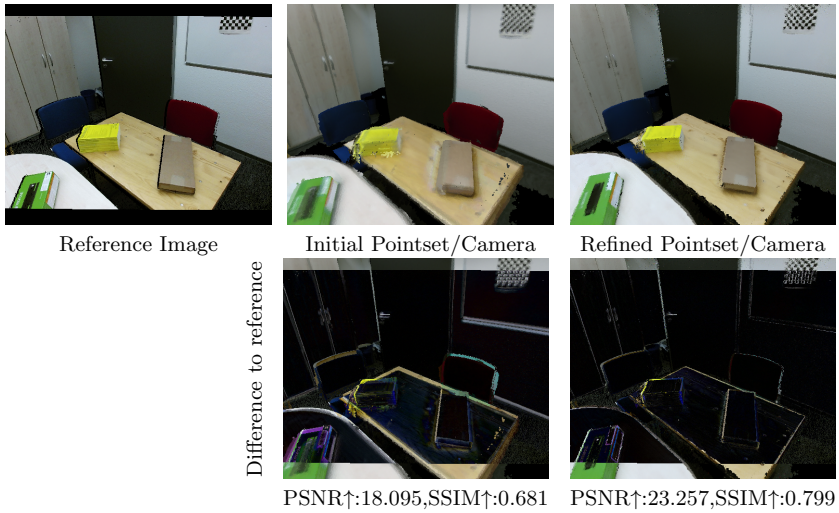

Fig. 4: Comparison between the reference image by Bode et al. [6], a rendered image from the initial SLAM reconstruction and a rendered image after refining the scene using our method. The masked areas in the reference image are a result of calibration and are not considered in the loss, PSNR or SSIM. The pixel-wise difference between the reference image and the rendered images is also depicted (darker values correspond to a smaller error). These highlight an improved alignment of the geometry with the reference image, the removal of outliers and the restoration of sharper textures after the refinement.

node combination required in Algorithm 1 by using a hash map. This map can be substantially smaller than the number of pixels times the number of points since the algorithm only needs to store the capacity of visited nodes. Additional details regarding our implementation are provided in the supplementary.

4 Applications and Results

We provide a qualitative and quantitative comparison between our method and previous differentiable point renderer in Figure 2 and Table 1. Furthermore, we demonstrate that our method can be applied to room-scale scenes with moderate hardware requirements (Figure 4) whereas DSS is unable to do so (Figure 5). Finally, we integrate our method into a neural rendering pipeline (Figure 3). Unless otherwise specified we use the "Adam" optimizer [28] with decay-rates $\beta_1 = 0.9$ and $\beta_2 = 0.999$ to minimize a simple L_1-image loss with a batch size of 12 without further regularization. The learning rate is initially set to be 0.01 and reduced 5 times by a factor of 2 at regular intervals during the 300 epochs. All experiments use $m = 40$ samples per pixel, an error threshold $\epsilon = 0.01$ and are run on a Nvidia GTX 1080 with 8GB VRAM. If points have no visual contribution from any viewing direction, the point is projected into the neighbourhood

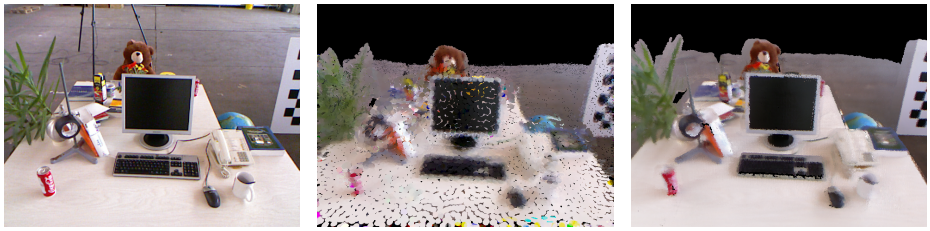

Reference Image | Refinement using DSS PSNR↑:15.412,SSIM↑:0.541 | Refinement using Ours PSNR↑:19.282,SSIM↑:0.683

Fig. 5: Comparison between the refinement of the SLAM reconstruction performed using either DSS or our proposed method. DSS [66] requires a downsampling by a factor of 10 to be run on the available hardware; DSS was also unable to align the pose correctly (compare the upper corner of the checkerboard).

of a randomly selected visible point. "Pulsar" [31] uses a similar technique but prunes non-contributing points which decreases the point cloud resolution.

Comparison - Image-based Shape Reconstruction To compare our method's ability to reconstruct shapes from images against previous point-based approaches, we use the dataset published in Yifan et al. [66]. Note that this dataset originally contained 5 objects, however, only 4 of them have been published. Based on the setup in [66], the images used for the shape reconstruction are rendered from the ground-truth point cloud with randomly sampled poses. For DSS [66] we compare against the results obtained using its published implementation [67]. For "SynSin" [61] and "Pulsar" [31] we use the implementations provided in [50] and apply them using our setup described in the previous paragraph.

The results in Figure 2 demonstrate that the proposed method is able to successfully reconstruct all objects. When comparing the results to reconstruction obtained with DSS, SynSin or Pulsar, it is apparent that the results obtained with our approach exhibit fewer outliers, holes in the surface and reconstructs smaller details more faithfully. The distances between the reconstructed and ground-truth point clouds reported in Table 1 emphasize that the improved reconstruction accuracy is not limited to the viewing direction in Figure 2. The proposed method achieves distances that are smaller by a factor of at least 2.9 and 2.8 for the Hausdorff and Chamfer distance when compared to previous methods and indicates more faithfully recovered shapes. For a additional comparisons and the runtime we refer to the supplementary.

Application - Room-scale Scene Refinement To demonstrate that our meth-od scales well to room-scale scenes, we utilize sequence RGB-D datasets by Steinbrucker et al. [59] and Bode et al. [6]. The latter registers RGB and depth measurements by masking RGB pixels which have no corresponding depth values. For the refinement we use point-based SLAM [26] to obtain an initial estimate for the point cloud and camera poses and optimize geometry, shading

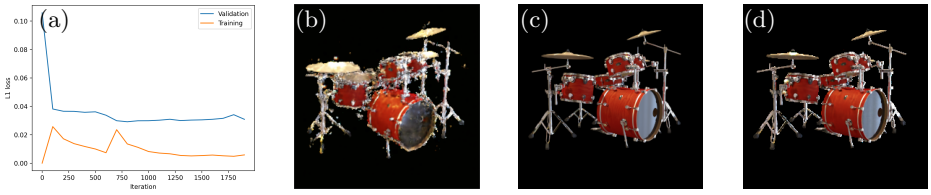

Fig. 6: The neural rendering framework suffers from overfitting, as indicated by the discrepancy between the training and validation loss curve (a). The neural renderer fails to reproduce certain test views (b) but is able to accurately reproduce its nearest training view; compare (c) and (d).

and camera parameters to improve the alignment between RGB images and observations using our method. Further details on this setup and results are provided in the supplementary. After the refinement, the SSIM improves by 17.33% compared to a frame rendered directly after SLAM reconstruction. The improvements exemplified in Figure 4 are a result of an improved pose alignment between frames and an improvement of shading and geometry. We would like to highlight the improved alignment of the table edge and the checkerboard pattern as a result of improved camera poses, which allows for sharper texture details. Furthermore, outliers near the table and chair were removed in the refinement using our method. In addition to the improvements of the camera poses, albedo values, and spherical harmonics coefficients, improvements to the geometry can be observed which contribute to the lower error. In contrast to "Adop" [55], which demonstrate a similar application, our method does not require training a network and avoids this overhead. We conduct the same experiments using DSS [66]. However, we found that DSS requires to downscale the point cloud by a factor of 10 to avoid out-of-memory exceptions on the used hardware. Figure 5 demonstrates that our method allows the refinement of room-scales scenes with higher fidelity compared to DSS on the same hardware.

Application - Neural Rendering To demonstrate the flexibility of our framework beyond shape reconstruction/refinement, we combine it with a neural shading network and train the model on the synthetic dataset by Mildenhall et al. [41]. The design of the neural shading pipeline follows an approach similar to Lassner and Zollhöfer [31]: The shading network is a U-Net generator and the model is trained to minimize an image loss and adversarial loss based on a Patch-GAN discriminator which we adapted from Isola et al. [19]. A detailed description of the initialization, architecture and all parameters is provided in the supplemental. Figure 3 depicts the results obtained by evaluating the trained model on the test split of the dataset. The neural shading network allows the model to render fine details for which the point cloud resolution would not suffice. However, the failure case in Figure 6 indicates that the neural shading model does not generalize equally well to every camera pose. Lassner and Zollhöfer [31] report a similar problem when demonstrating "Pulsar" as part of their neural rendering model.

#Samples	HD ↓	CD ↓
1	8.287	6.766
3	8.87	3.532
5	8.189	2.717
20	1.07	0.105
40	0.442	0.125

Table 2: Influence of the number of samples on Hausdorff and Chamfer distance.

#Views	HD ↓	CD ↓
16	49.159	20.138
64	1.097	0.156
124	0.442	0.125
300	0.409	0.13

Table 3: Influence of the number of views on Hausdorff and Chamfer distance.

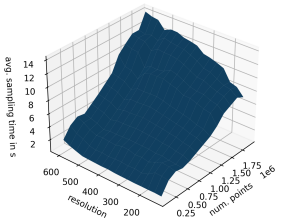

Fig. 7: Linear scaling of the our algorithm with respect to instance size.

This suggests that overfitting is not a problem of our renderer but a limitation of neural shading models.

Scaling and Ablation To study the effect of the user-defined parameters on the shape recovery results, we use the results on the bunny dataset as a baseline. We report the effect of the per-pixel sample size m in Table 2 and the algorithm's robustness with respect to the number of viewing direction in Table 3. While increasing the sample size improves the reconstruction, a sample size beyond 40 is not possible in our implementation since it is constraint by the amount of shared memory. We found that increasing the number of views beyond 100 does result in significant improvements on this scene. We further demonstrate that Algorithm 1 scales linearly with respect to the number of points and pixels in Figure 7. We provide a more detailed study of the runtime in the supplementary.

5 Conclusion

Our stochastic framework for differentiable point-rendering addresses the inherent bias or locality in the gradient computation of previous methods by deriving an unbiased gradient estimator. To evaluate this estimator we introduce a near linear-time algorithm to perform efficient sampling in image space. We empirically verified that our proposed method enables more faithful image-based object reconstruction without relying on regularization. Furthermore, we demonstrated the scalability and flexibility of our approach by its application for room-scale scene refinement and integrating it into a neural rendering pipeline.

Future Work Although the current implementation of the sampling algorithm is hardware-agnostic, we anticipate that the integration into a hardware-accelerated rendering pipeline may be beneficial. This is in light of recent developments in neural implicit representations [42], which have significantly improved their efficiency. We believe that reducing the hardware requirements makes methods more accessible and can yield more energy-efficient models.

Acknowledgments This work was partially funded by the DFG (German Research Foundation) KL 1142/11-2 (FOR 2535 Anticipating Human Behavior).

References

1. Aberman, K., Shi, M., Liao, J., Lischinski, D., Chen, B., Cohen-Or, D.: Deep video-based performance cloning. In: Computer Graphics Forum. vol. 38, pp. 219–233. Wiley Online Library (2019)
2. Aliev, K.A., Sevastopolsky, A., Kolos, M., Ulyanov, D., Lempitsky, V.: Neural point-based graphics. In: Computer Vision–ECCV 2020: 16th European Conference, Glasgow, UK, August 23–28, 2020, Proceedings, Part XXII 16. pp. 696–712. Springer (2020)
3. Bangaru, S.P., Li, T.M., Durand, F.: Unbiased warped-area sampling for differentiable rendering. ACM Transactions on Graphics (TOG) **39**(6), 1–18 (2020)
4. Beigpour, S., Kolb, A., Kunz, S.: A comprehensive multi-illuminant dataset for benchmarking of intrinsic image algorithms. In: Proc. IEEE International Conference on Computer Vision (ICCV). pp. 172–180 (12 2015)
5. Bell, N., Hoberock, J.: Thrust: A productivity-oriented library for cuda. In: GPU computing gems Jade edition, pp. 359–371. Elsevier (2012)
6. Bode, L., Merzbach, S., Stotko, P., Weinmann, M., Klein, R.: Real-time multi-material reflectance reconstruction for large-scale scenes under uncontrolled illumination from rgb-d image sequences. In: 2019 International Conference on 3D Vision (3DV). pp. 709–718. IEEE (2019)
7. Boss, M., Braun, R., Jampani, V., Barron, J.T., Liu, C., Lensch, H.: Nerd: Neural reflectance decomposition from image collections. In: Proceedings of the IEEE/CVF International Conference on Computer Vision. pp. 12684–12694 (2021)
8. Bozic, A., Zollhofer, M., Theobalt, C., Nießner, M.: Deepdeform: Learning non-rigid rgb-d reconstruction with semi-supervised data. In: Proceedings of the IEEE/CVF Conference on Computer Vision and Pattern Recognition. pp. 7002–7012 (2020)
9. Brewer, K.R., Early, L., Joyce, S.: Selecting several samples from a single population. Australian Journal of Statistics **14**(3), 231–239 (1972)
10. Chen, W., Ling, H., Gao, J., Smith, E., Lehtinen, J., Jacobson, A., Fidler, S.: Learning to predict 3d objects with an interpolation-based differentiable renderer. Advances in Neural Information Processing Systems **32**, 9609–9619 (2019)
11. Curtin, R., March, W., Ram, P., Anderson, D., Gray, A., Isbell, C.: Tree-independent dual-tree algorithms. In: International Conference on Machine Learning. pp. 1435–1443. PMLR (2013)
12. Dave, C.P., Joshi, R., Srivastava, S.: A survey on geometric correction of satellite imagery. International Journal of Computer Applications **116**(12) (2015)
13. Garbin, S.J., Kowalski, M., Johnson, M., Shotton, J., Valentin, J.: Fastnerf: High-fidelity neural rendering at 200fps. In: Proceedings of the IEEE/CVF International Conference on Computer Vision. pp. 14346–14355 (2021)
14. Greengard, L., Huang, J., Rokhlin, V., Wandzura, S.: Accelerating fast multipole methods for the helmholtz equation at low frequencies. IEEE Computational Science and Engineering **5**(3), 32–38 (1998)
15. Greengard, L., Strain, J.: The fast gauss transform. SIAM Journal on Scientific and Statistical Computing **12**(1), 79–94 (1991)
16. Heckbert, P.S.: Fundamentals of texture mapping and image warping (1989)
17. Henzler, P., Mitra, N.J., Ritschel, T.: Escaping plato's cave: 3d shape from adversarial rendering. In: Proceedings of the IEEE/CVF International Conference on Computer Vision. pp. 9984–9993 (2019)

18. Insafutdinov, E., Dosovitskiy, A.: Unsupervised learning of shape and pose with differentiable point clouds. arXiv preprint arXiv:1810.09381 (2018)
19. Isola, P., Zhu, J.Y., Zhou, T., Efros, A.A.: Image-to-image translation with conditional adversarial networks. In: Proceedings of the IEEE conference on computer vision and pattern recognition. pp. 1125–1134 (2017)
20. Jiang, Y., Ji, D., Han, Z., Zwicker, M.: Sdfdiff: Differentiable rendering of signed distance fields for 3d shape optimization. In: Proceedings of the IEEE/CVF Conference on Computer Vision and Pattern Recognition. pp. 1251–1261 (2020)
21. Kappel, M., Golyanik, V., Elgharib, M., Henningson, J.O., Seidel, H.P., Castillo, S., Theobalt, C., Magnor, M.: High-fidelity neural human motion transfer from monocular video. In: Proceedings of the IEEE/CVF Conference on Computer Vision and Pattern Recognition. pp. 1541–1550 (2021)
22. Karras, T.: Maximizing parallelism in the construction of bvhs, octrees, and k-d trees. In: Proceedings of the Fourth ACM SIGGRAPH/Eurographics conference on High-Performance Graphics. pp. 33–37 (2012)
23. Kato, H., Beker, D., Morariu, M., Ando, T., Matsuoka, T., Kehl, W., Gaidon, A.: Differentiable rendering: A survey. arXiv preprint arXiv:2006.12057 (2020)
24. Kato, H., Harada, T.: Learning view priors for single-view 3d reconstruction. In: Proceedings of the IEEE/CVF Conference on Computer Vision and Pattern Recognition. pp. 9778–9787 (2019)
25. Kato, H., Ushiku, Y., Harada, T.: Neural 3d mesh renderer. In: Proceedings of the IEEE conference on computer vision and pattern recognition. pp. 3907–3916 (2018)
26. Keller, M., Lefloch, D., Lambers, M., Izadi, S., Weyrich, T., Kolb, A.: Real-time 3d reconstruction in dynamic scenes using point-based fusion. In: 2013 International Conference on 3D Vision-3DV 2013. pp. 1–8. IEEE (2013)
27. Kim, H., Garrido, P., Tewari, A., Xu, W., Thies, J., Niessner, M., Pérez, P., Richardt, C., Zollhöfer, M., Theobalt, C.: Deep video portraits. ACM Transactions on Graphics (TOG) **37**(4), 1–14 (2018)
28. Kingma, D.P., Ba, J.: Adam: A method for stochastic optimization. arXiv preprint arXiv:1412.6980 (2014)
29. Kopanas, G., Philip, J., Leimkühler, T., Drettakis, G.: Point-based neural rendering with per-view optimization. In: Computer Graphics Forum. vol. 40, pp. 29–43. Wiley Online Library (2021)
30. Laine, S., Hellsten, J., Karras, T., Seol, Y., Lehtinen, J., Aila, T.: Modular primitives for high-performance differentiable rendering. ACM Transactions on Graphics (TOG) **39**(6), 1–14 (2020)
31. Lassner, C., Zollhofer, M.: Pulsar: Efficient sphere-based neural rendering. In: Proceedings of the IEEE/CVF Conference on Computer Vision and Pattern Recognition. pp. 1440–1449 (2021)
32. Lee, D., Moore, A.W., Gray, A.G.: Dual-tree fast gauss transforms. In: Advances in Neural Information Processing Systems. pp. 747–754 (2006)
33. Li, L., Zhu, S., Fu, H., Tan, P., Tai, C.L.: End-to-end learning local multi-view descriptors for 3d point clouds. In: Proceedings of the IEEE/CVF Conference on Computer Vision and Pattern Recognition. pp. 1919–1928 (2020)
34. Lin, C.H., Kong, C., Lucey, S.: Learning efficient point cloud generation for dense 3d object reconstruction. In: proceedings of the AAAI Conference on Artificial Intelligence. vol. 32 (2018)
35. Lingg, M.P., Hughey, S.M., Dikbayir, D., Shanker, B., Aktulga, H.M.: Exploring task parallelism for the multilevel fast multipole algorithm. In: 2020 IEEE 27th

International Conference on High Performance Computing, Data, and Analytics (HiPC). pp. 41–50. IEEE (2020)
36. Liu, S., Li, T., Chen, W., Li, H.: Soft rasterizer: A differentiable renderer for image-based 3d reasoning. In: Proceedings of the IEEE/CVF International Conference on Computer Vision. pp. 7708–7717 (2019)
37. Lombardi, S., Simon, T., Saragih, J., Schwartz, G., Lehrmann, A., Sheikh, Y.: Neural volumes: Learning dynamic renderable volumes from images. arXiv preprint arXiv:1906.07751 (2019)
38. Lombardi, S., Simon, T., Schwartz, G., Zollhoefer, M., Sheikh, Y., Saragih, J.: Mixture of volumetric primitives for efficient neural rendering. arXiv preprint arXiv:2103.01954 (2021)
39. Loper, M.M., Black, M.J.: Opendr: An approximate differentiable renderer. In: European Conference on Computer Vision. pp. 154–169. Springer (2014)
40. Luan, F., Zhao, S., Bala, K., Dong, Z.: Unified shape and svbrdf recovery using differentiable monte carlo rendering. arXiv preprint arXiv:2103.15208 (2021)
41. Mildenhall, B., Srinivasan, P.P., Tancik, M., Barron, J.T., Ramamoorthi, R., Ng, R.: Nerf: Representing scenes as neural radiance fields for view synthesis. In: European conference on computer vision. pp. 405–421. Springer (2020)
42. Müller, T., Evans, A., Schied, C., Keller, A.: Instant neural graphics primitives with a multiresolution hash encoding. arXiv preprint arXiv:2201.05989 (2022)
43. Nimier-David, M., Speierer, S., Ruiz, B., Jakob, W.: Radiative backpropagation: an adjoint method for lightning-fast differentiable rendering. ACM Transactions on Graphics (TOG) **39**(4), 146–1 (2020)
44. Nimier-David, M., Vicini, D., Zeltner, T., Jakob, W.: Mitsuba 2: A retargetable forward and inverse renderer. ACM Transactions on Graphics (TOG) **38**(6), 1–17 (2019)
45. Ohlsson, E.: Sequential poisson sampling. Journal of official Statistics **14**(2), 149 (1998)
46. Paszke, A., Gross, S., Massa, F., Lerer, A., Bradbury, J., Chanan, G., Killeen, T., Lin, Z., Gimelshein, N., Antiga, L., et al.: Pytorch: An imperative style, high-performance deep learning library. Advances in neural information processing systems **32**, 8026–8037 (2019)
47. Patow, G., Pueyo, X.: A survey of inverse rendering problems. In: Computer graphics forum. vol. 22, pp. 663–687. Wiley Online Library (2003)
48. Petersen, F., Bermano, A.H., Deussen, O., Cohen-Or, D.: Pix2vex: Image-to-geometry reconstruction using a smooth differentiable renderer. arXiv preprint arXiv:1903.11149 (2019)
49. Poursaeed, O., Fisher, M., Aigerman, N., Kim, V.G.: Coupling explicit and implicit surface representations for generative 3d modeling. In: European Conference on Computer Vision. pp. 667–683. Springer (2020)
50. Ravi, N., Reizenstein, J., Novotny, D., Gordon, T., Lo, W.Y., Johnson, J., Gkioxari, G.: Accelerating 3d deep learning with pytorch3d. arXiv preprint arXiv:2007.08501 (2020)
51. Reiser, C., Peng, S., Liao, Y., Geiger, A.: Kilonerf: Speeding up neural radiance fields with thousands of tiny mlps. In: Proceedings of the IEEE/CVF International Conference on Computer Vision. pp. 14335–14345 (2021)
52. Rhodin, H., Robertini, N., Richardt, C., Seidel, H.P., Theobalt, C.: A versatile scene model with differentiable visibility applied to generative pose estimation. In: Proceedings of the IEEE International Conference on Computer Vision. pp. 765–773 (2015)

53. Rossler, A., Cozzolino, D., Verdoliva, L., Riess, C., Thies, J., Nießner, M.: Faceforensics++: Learning to detect manipulated facial images. In: Proceedings of the IEEE/CVF International Conference on Computer Vision. pp. 1–11 (2019)
54. Roveri, R., Rahmann, L., Oztireli, C., Gross, M.: A network architecture for point cloud classification via automatic depth images generation. In: Proceedings of the IEEE Conference on Computer Vision and Pattern Recognition. pp. 4176–4184 (2018)
55. Rückert, D., Franke, L., Stamminger, M.: Adop: Approximate differentiable one-pixel point rendering. arXiv preprint arXiv:2110.06635 (2021)
56. Ryan, J.P., Ament, S., Gomes, C.P., Damle, A.: The fast kernel transform. arXiv preprint arXiv:2106.04487 (2021)
57. Sengupta, S.: Constraints and Priors for Inverse Rendering from Limited Observations. Ph.D. thesis, University of Maryland, College Park (2019)
58. Srinivasan, P.P., Deng, B., Zhang, X., Tancik, M., Mildenhall, B., Barron, J.T.: Nerv: Neural reflectance and visibility fields for relighting and view synthesis. In: Proceedings of the IEEE/CVF Conference on Computer Vision and Pattern Recognition. pp. 7495–7504 (2021)
59. Steinbrücker, F., Sturm, J., Cremers, D.: Real-time visual odometry from dense rgb-d images. In: 2011 IEEE international conference on computer vision workshops (ICCV Workshops). pp. 719–722. IEEE (2011)
60. Tulsiani, S., Zhou, T., Efros, A.A., Malik, J.: Multi-view supervision for single-view reconstruction via differentiable ray consistency. In: Proceedings of the IEEE conference on computer vision and pattern recognition. pp. 2626–2634 (2017)
61. Wiles, O., Gkioxari, G., Szeliski, R., Johnson, J.: Synsin: End-to-end view synthesis from a single image. In: Proceedings of the IEEE/CVF Conference on Computer Vision and Pattern Recognition. pp. 7467–7477 (2020)
62. Wilson, L., Vaughn, N., Krasny, R.: A gpu-accelerated fast multipole method based on barycentric lagrange interpolation and dual tree traversal. Computer Physics Communications **265**, 108017 (2021)
63. Xian, W., Huang, J.B., Kopf, J., Kim, C.: Space-time neural irradiance fields for free-viewpoint video. In: Proceedings of the IEEE/CVF Conference on Computer Vision and Pattern Recognition. pp. 9421–9431 (2021)
64. Yan, X., Yang, J., Yumer, E., Guo, Y., Lee, H.: Perspective transformer nets: Learning single-view 3d object reconstruction without 3d supervision. arXiv preprint arXiv:1612.00814 (2016)
65. Yang, C., Duraiswami, R., Gumerov, N.A., Davis, L.: Improved fast gauss transform and efficient kernel density estimation. In: Computer Vision, IEEE International Conference on. vol. 2, pp. 464–464. IEEE Computer Society (2003)
66. Yifan, W., Serena, F., Wu, S., Öztireli, C., Sorkine-Hornung, O.: Differentiable surface splatting for point-based geometry processing. ACM Transactions on Graphics (TOG) **38**(6), 1–14 (2019)
67. Yifan, W., Serena, F., Wu, S., Öztireli, C., Sorkine-Hornung, O.: Github - yifita/dss: Differentiable surface splatting (2019), `https://github.com/yifita/DSS/tree/44732f9b771ca7e5ee4cfebeaf8528be1d097e3e`
68. Yokota, R.: An fmm based on dual tree traversal for many-core architectures. Journal of Algorithms & Computational Technology **7**(3), 301–324 (2013)
69. Yu, A., Fridovich-Keil, S., Tancik, M., Chen, Q., Recht, B., Kanazawa, A.: Plenoxels: Radiance fields without neural networks. arXiv preprint arXiv:2112.05131 (2021)
70. Yu, A., Li, R., Tancik, M., Li, H., Ng, R., Kanazawa, A.: Plenoctrees for real-time rendering of neural radiance fields. arXiv preprint arXiv:2103.14024 (2021)

71. Zakharov, E., Shysheya, A., Burkov, E., Lempitsky, V.: Few-shot adversarial learning of realistic neural talking head models. In: Proceedings of the IEEE/CVF International Conference on Computer Vision. pp. 9459–9468 (2019)
72. Zeltner, T., Speierer, S., Georgiev, I., Jakob, W.: Monte carlo estimators for differential light transport. ACM Transactions on Graphics (TOG) **40**(4), 1–16 (2021)
73. Zhang, C., Miller, B., Yan, K., Gkioulekas, I., Zhao, S.: Path-space differentiable rendering. ACM transactions on graphics **39**(4) (2020)
74. Zhou, H., Sun, Y., Wu, W., Loy, C.C., Wang, X., Liu, Z.: Pose-controllable talking face generation by implicitly modularized audio-visual representation. In: Proceedings of the IEEE/CVF Conference on Computer Vision and Pattern Recognition. pp. 4176–4186 (2021)
75. Zhu, J.Y., Zhang, Z., Zhang, C., Wu, J., Torralba, A., Tenenbaum, J.B., Freeman, W.T.: Visual object networks: Image generation with disentangled 3d representation. arXiv preprint arXiv:1812.02725 (2018)
76. Zhu, R., Kiani Galoogahi, H., Wang, C., Lucey, S.: Rethinking reprojection: Closing the loop for pose-aware shape reconstruction from a single image. In: Proceedings of the IEEE International Conference on Computer Vision. pp. 57–65 (2017)
77. Zwicker, M., Pfister, H., Van Baar, J., Gross, M.: Surface splatting. In: Proceedings of the 28th annual conference on Computer graphics and interactive techniques. pp. 371–378 (2001)
78. Zwicker, M., Pfister, H., Van Baar, J., Gross, M.: Ewa splatting. IEEE Transactions on Visualization and Computer Graphics **8**(3), 223–238 (2002)